HEFAT2014
10th International Conference on Heat Transfer, Fluid Mechanics and Thermodynamics
14 – 16 July 2014
Orlando, Florida

TRANSIENT PERFORMANCE INVESTIGATION OF DIFFERENT FLOW-FIELD DESIGNS OF AUTOMOTIVE POLYMER ELECTROLYTE MEMBRANE FUEL CELL (PEMFC) USING COMPUTATIONAL FLUID DYNAMICS (CFD)

Choopanya P.* and Yang Z.
*Author for correspondence
Department of Engineering and Design,
University of Sussex,
Brighton, BN1 9QT,
United Kingdom,
E-mail: p.choopanya@sussex.ac.uk

ABSTRACT

Transient performance of a polymer electrolyte membrane (PEM) fuel cell in terms of the time-dependent current density profile that responds to the varying cell potential is of critical importance for an automotive PEM fuel cell. A step change in cell potential is applied to the cell terminals to simulate a sudden change in load demand due to an engine startup or very high acceleration. The transient responses of the three most commonly used flow-fields, namely, parallel, single-serpentine, and interdigitated designs in terms of the magnitude of current overshoot and time taken to adjust to the new equilibrium state are compared. The results suggest the serpentine flow-field outperforms its two counterparts as it balances the satisfactory transient performance with an expense of acceptable pressure drop across the cell and hence it is the most appropriate design to be used in automotive PEM fuel cells.

INTRODUCTION

A fuel cell is an electrochemical device that converts chemical energy into electricity by utilising the reversed process of water electrolysis where heat and water are the only by-products. Among its fuel cell family, a PEMFC is drawing most interests from the research community as a clean and efficient technology for power generation, especially in the automobile industry. Its merits include a simple structure, relatively high current and power densities that allow for a light-weight and compact system which is of paramount importance in vehicle applications, and a low operating temperature is desirable for a quick start characteristic and fast transient response. In addition its quiet operation will become more and more important as regulations on noise generation will become more stringent.

As emphasised in the work of Djilali [1], an insight into the highly coupled, non-linear transport phenomena and electrochemistry of a fuel cell is crucial and PEMFC modelling therefore plays an important role in improving our understanding of what is happening inside a cell since the typical length scale of a few microns to millimetres poses severe difficulties to carry out experimental work. An excellent guidance on the fundamentals of fuel cell modelling was given by C. Y. Wang [2] and reviews of PEMFC modelling [3-5] in many different aspects also exist in the literature.

The very first models were proposed by Springer et al. [6] and Bernardi et al. [7-8] in which the transport of gases through the porous diffusion layer and membrane was modelled in a pseudo 1-dimensional approach. Despite their 1-dimensional nature, they were the stepping-stone to PEMFC modelling, leading to more complete and complex, multi-dimensional models. Two-dimensional works [9-13] were also published focusing on different aspects of the cell. A remarkable work was proposed by Gurau et al. [14] in which a 2-dimensional model was developed using a single-domain approach since the governing equations for all regions are similar and can be written in a generic convective-diffusive transport equation form, allowing for the exploitation of the computational fluid dynamics (CFD) technique and leading to the computational fuel cell dynamics (CFCD) method which was first demonstrated in the work [15-16]. Dutta et al. [17] developed a 3-dimensional PEMFC model for the first time based on a commercial CFD code which was modified to account for the electrochemistry aspect of the cell.

Nevertheless, such proposed models only describe a steady-state performance where in practical applications, however, especially for an automotive application, a fuel cell is often continuously exposed to load changes due to different power demands and hence the study of the transient performance is essential but few studies have been carried out in this area. It has been realised through the work of many researchers both experimentally [18-21] and numerically [22-41] that when the applied cell voltage is varied, the responding cell current is

always accompanied with some degree of under/overshoots before approaching the new steady state.

Moreover, the magnitude of the under/overshoot and time depend on many factors, for example temperature [22, 37], reactant gases humidity [26, 29, 36]. A series of comprehensive numerical studies on the effect of fuel/air stoichiometries on transient performance were also published by Shimpalee et al. [27-28]. However, most dynamic models used a simple, straight single-channel representation of the entire cell with only a few paying attention to more realistic flow-fields [30, 31, 33, 38] and their geometrical effect on the transient performance.

It is, therefore, the objective of this study to develop a cell-level, dynamic PEM fuel cell model that is capable of predicting transient behaviour of the three most-commonly used flow-fields; straight-parallel, serpentine, and interdigitated. The complex interplay between many in-channel parameters such as gas temperature, pressure and concentration will be made available and hence the geometrical influence of the flow-field can be thoroughly understood. This will allow engineers and designers to achieve a better flow-field design from a transient performance point of view.

ABBREVIATIONS

CFCD	Computational fuel cell dynamics
CFD	Computational fluid dynamics
CL	Catalyst layer
GDL	Gas diffusion layer
MEA	Membrane electrode assembly
PEM	Polymer electrolyte membrane

NOMENCLATURE

a	[-]	*Liquid water activity*
	[m^2]	Area
C_i	[$kmolm^{-3}$]	Local molar concentration of species *i*
$D_{\vec{j},i}$	[m^2s^{-1}]	Diffusion coefficient of species *i*, in *j* direction
E	[Jkg^{-1}]]	Specific total energy
F	[$Cmol^{-1}$]	Faraday's constant, 96487
h_0	[Jkg^{-1}]	Specific total enthalpy
I	[Am^{-2}]	Local current density
i	[Jkg^{-1}]	Specific internal energy
$J_{\vec{j},i}$	[$kgm^{-2}s^{-1}$]	Diffusional mass flux of species *i*, in *j* direction
j_{an}^{ref}, j_{ca}^{ref}	[Am^{-2}]	Reference exchange current density
K	[m^2]	Permeability
k	[$Wm^{-1}K^{-1}$]	Thermal conductivity
M	[$kgkmol^{-1}$]	Molar mass
n_d	[-]	Osmotic drag coefficient
P	[Pa]	Pressure
R	[$Jmol^{-1}K^{-1}$]	Universal gas constant, 8.314
$R_{an,ca}$	[Am^{-3}]	Transfer current density
r_w	[$kgm^{-3}s^{-1}$]	Liquid water condensation rate
s	[-]	Liquid water saturation
T	[K]	Absolute temperature
$\vec{V}$	[ms^{-1}]	Velocity vector
x_i	[-]	Mass fraction of species *i*
y_i	[-]	Mole fraction of species *i*

Greek characters

α	[-]	Charge transfer coefficient
β	[m^2]	Permeability of porous media
γ	[-]	Concentration parameter
ε	[-]	Porosity
η	[V]	Overpotential
λ	[-]	Membrane water content (water molecules per sulphuric acid group in the membrane)
μ	[Pa-s]	Viscous coefficient
ξ	[-]	Stoichiometric ratio
ρ	[kgm^{-3}]	Density
ς	[m^{-1}]	Specific active surface area
σ	[$\Omega^{-1}m^{-1}$]	Electrical conductivity
τ	[Nm^{-2}]	Stress tensor
φ	[V]	Potential

Subscripts

an	Anode
aw	Anode water vapour
ca	Cathode
cw	Cathode water vapour
liquid	Liquid phase
mem	Membrane phase
ref	Reference
sat	Saturation
sol	Solid phase

MODEL DEVELOPMENT

Computational Domains

Figure 1 shows the three different cell designs; parallel (A), serpentine (B), and interdigitated (C). A current collector is excluded hence each cell comprises of 7 layers;

$$CH_{an} \parallel GDL_{an} \parallel CL_{an} \parallel PEM \parallel CL_{ca} \parallel GDL_{ca} \parallel CH_{ca}$$

A side view of the fuel cell is also given to demonstrate how all layers are assembled into a single cell (not to scale). The active area of the cells are approximately 0.0004 m^2 and **Table 1** gives the exact geometrical parameters of each fuel cell.

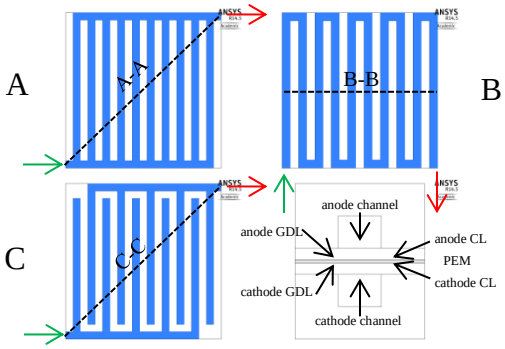

Figure 1 Three different cell designs; green – inlet, red – outlet

Table 1 Cell dimensions

Parameter	A	B	C
Cell width [mm]	21	19	21
Cell length [mm]	21	19	21
Channel width [mm]	1	1	1
Channel height [mm]	1	1	1
Rib width [mm]	1	1	1
GDL (Toray 120) thickness [µm]	370	370	370
CL thickness [µm]	20	20	20
PEM (Nafion 117) thickness [µm]	178	178	178
Active surface area [cm^2]	4.41	3.61	4.41

Modelling Assumptions

1. Laminar channel flows at the outlets of both anode and cathode channels are assumed.
2. Two-phase flow within channels, GDLs, and CLs; water presents in both liquid and vapour form depending on the local saturation value.
3. The anode gas comprises of hydrogen and water vapour and air (oxygen, nitrogen, and water vapour) for the cathode. All gases are behaving as ideal gases.
4. Reactant gases are fully humidified ($RH\%_{a,c}$ = 100%)
5. The GDLs, CLs, and membrane are isotropic and homogenous.
6. The membrane is impermeable to the reactant gases (no fuel cross-over).
7. The potential drop over the cell terminals is negligible (constant potentials over the terminals) due to high electrical conductivity.

Governing Equations

Based on the model used by Choopanya and Peng [42-43], the transient nature of the PEM fuel cell is taken into account by including the time-dependent term in the governing equations as follow:

1. Conservation of Mass

$$\varepsilon\frac{\partial\rho}{\partial t}+\nabla\cdot\left(\rho\vec{V}\right)=S_m \tag{1}$$

The source term, S_m accounts for the consumption or generation of reactant gases at the anode and cathode catalyst layers and it is zero in other layers.

At anode CL; $S_m = S_{H_2} + S_{aw}$ (2)

At cathode CL; $S_m = S_{O_2} + S_{cw}$ (3)

Where $S_{H_2} = -\frac{M_{H_2}}{2F}R_{an}$ (4)

$$S_{aw} = -\frac{\alpha M_{H_2O}}{F}R_{an} \tag{5}$$

$$S_{O_2} = -\frac{M_{O_2}}{4F}R_{ca} \tag{6}$$

$$S_{cw} = \frac{(1+2\alpha)M_{H_2O}}{2F}R_{ca} \tag{7}$$

2. Conservation of Momentum

$$\frac{1}{\varepsilon}\frac{\partial\left(\rho\vec{V}\right)}{\partial t}+\frac{1}{\varepsilon^2}\nabla\cdot\left(\rho\vec{V}\vec{V}\right)=-\nabla p+\nabla\bar{\bar{\tau}}+S_{p\vec{j}} \tag{8}$$

Where $\vec{j}$ represents *x*-, *y*-, and *z*-coordinates

$$S_{px}=-\frac{\mu}{\beta_x}u,\ S_{py}=-\frac{\mu}{\beta_y}v,\ S_{pz}=-\frac{\mu}{\beta_z}w \tag{9a-9c}$$

Similarly, the source terms, S_{px}, S_{py}, and S_{pz} are modelled using Darcy's Law and equal to zero in all layers except the MEA to account for the effect of porous materials. Since the gas diffusion layers, catalyst layers, and membrane are assumed isotropic and homogenous, hence $\beta_x = \beta_y = \beta_z = \beta$.

3. Conservation of Species

The subscript *i* represents hydrogen, anode water vapour, oxygen, and cathode water vapour.

$$\varepsilon\frac{\partial(\rho x_i)}{\partial t}+\nabla\cdot\left(\rho x_i\vec{V}\right)=\nabla J_{\vec{j},i}+S_i \tag{10}$$

Mass fraction of nitrogen; $x_{N_2} = 1 - x_{O_2} - x_{cw}$ (11)

Again, S_{H_2} and S_{aw}, S_{O_2} and S_{cw} are source terms at anode and cathode catalyst layers, respectively. The diffusion mass flux of a species *i* in the *j* direction is given as,

$$J_{\vec{j},i} = -\rho D_{\vec{j},i}\frac{\partial x_i}{\partial\vec{j}} \tag{12}$$

The diffusion coefficient is defined as;

$$\begin{aligned} D_i &= \varepsilon^{1.5}(1-s)^{\gamma_s}D_i^0\left(\frac{p_0}{p}\right)^{\gamma_p}\left(\frac{T}{T_0}\right)^{\gamma_t} \\ &= \varepsilon^{1.5}(1-s)^{\gamma_s}D_i^0\left(\frac{101325}{p}\right)\left(\frac{T}{300}\right)^{1.5} \end{aligned} \tag{13}$$

4. Conservation of energy

Heat transfer in the PEMFC is modelled through the total enthalpy (h_0) equation;

$$\begin{aligned} &\varepsilon\frac{\partial(\rho h_0)}{\partial t}+\nabla\cdot\left(\rho h_0\vec{V}\right)=\nabla\cdot(k\nabla T)+\frac{\partial(u\tau_{xx})}{\partial x}+\frac{\partial(u\tau_{yx})}{\partial y}+\frac{\partial(u\tau_{zx})}{\partial z} \\ &+\frac{\partial(v\tau_{xy})}{\partial x}+\frac{\partial(v\tau_{yy})}{\partial y}+\frac{\partial(v\tau_{zy})}{\partial z}+\frac{\partial(w\tau_{xz})}{\partial x}+\frac{\partial(w\tau_{yz})}{\partial y}+\frac{\partial(w\tau_{zz})}{\partial z}+S_h \end{aligned} \tag{14}$$

Where $h_0 = i + \frac{p}{\rho} + \frac{1}{2}\left(u^2+v^2+w^2\right) = E + \frac{p}{\rho}$ (15)

Additional heat sources are needed to account for the irreversibility due to the fact that all chemical energy cannot be converted into electrical energy. This is expressed as;

$$S_h = h_{react} - R_{an,ca}\eta_{an,ca} + I^2R_{Ohm} + h_L \tag{16}$$

Where h_{react} is the net enthalpy change due to electrochemical reactions, $R_{an,ca}\eta_{an,ca}$ is the product of transfer current and overpotential in anode/cathode triple-phase-boundary, TPB, and h_L is the enthalpy change due to water condensation/evaporation.

5. Conservation of charge

The driving force for an electrochemical reaction is the surface overpotential - the difference between the phase potential of the solid and phase potential of electrolyte/membrane. Therefore two additional equations are to be solved. These are the potential equation for electron transport through the solid conductive materials (current collectors and solid grids of the porous media) and potential equation for protonic transport through the electrode/membrane and are shown, respectively.

$$\frac{\partial\eta}{\partial t}+\nabla\cdot(\sigma_{sol}\nabla\varphi_{sol})+R_{sol}=0 \tag{17}$$

$$\frac{\partial\eta}{\partial t}+\nabla\cdot(\sigma_{mem}\nabla\varphi_{mem})+R_{mem}=0 \tag{18}$$

The source terms represent the transfer currents within the catalyst layers and are expressed by Butler-Volmer Equation;

$$R_{an} = \left(\zeta_{an}j_{an}^{ref}\right)\left(\frac{C_{H_2}}{C_{H_2,ref}}\right)^{\gamma_{an}}\left(e^{\frac{\alpha_{an}F\eta_{an}}{RT}}-e^{\frac{-\alpha_{ca}F\eta_{an}}{RT}}\right) \tag{19}$$

$$R_{ca} = \left(\zeta_{ca}j_{ca}^{ref}\right)\left(\frac{C_{O_2}}{C_{O_2,ref}}\right)^{\gamma_{ca}}\left(-e^{\frac{\alpha_{an}F\eta_{ca}}{RT}}+e^{\frac{-\alpha_{ca}F\eta_{ca}}{RT}}\right) \tag{20}$$

6. Water saturation

The liquid water formation and transport is governed by the following conservation of volume fraction of liquid water, or the water saturation;

$$\nabla\cdot\left(\rho_l\vec{V}_l s\right)=r_w \qquad (21)$$

The subscript l stands for liquid water and r_w is the liquid water condensation rate and is a function of the difference between water vapour pressure and saturation pressure. In order to correctly model the effect of porous media, the convective term in **Equation 21** must be modified to include the effect of capillary force and this transforms to

$$\nabla\cdot\left(\rho_l\frac{Ks^3}{\mu_l}\frac{dp_c}{ds}\nabla s\right)=r_w \qquad (22)$$

Where p_c is the capillary pressure determined as a function of s according to the Leverett function.

7. Transport of water inside the membrane

There exist two types of transport mechanism of water in the membrane; electro-osmotic drag of water molecule by protons from anode to cathode and back-diffusion of water from cathode to anode due to concentration gradient of water between the two sides. The net water flux across the membrane is expressed as the balance between these two mechanisms.

Osmotic drag coefficient; $n_d=2.5\times\frac{\lambda}{22}$ (23)

Back-diffusion flux; $J_w^{diff}=-\frac{\rho_{mem}}{M_{mem}}M_{H_2O}D_l\nabla\lambda$ (24)

Membrane water diffusivity; $D_l=f(\lambda)e^{2416\left(\frac{1}{303}-\frac{1}{T}\right)}$ (25)

Membrane water content can be calculated by using;

$$\lambda=0.043+17.18a-39.85a^2+36a^3 \quad \text{if a < 1}$$
$$\lambda=14+1.4(a-1) \quad \text{if a > 1} \qquad (26)$$

The water activity, $a=\frac{p_{wv}}{p_{sat}}+2s$ (27)

The water vapour pressure; $p_{wv}=y_{H_2O}p$ (28)

Saturation pressure,

$$\log_{10}p_{sat}=-2.1794+0.02953(T-273.15)-9.1837\times10^{-5}(T-273.15)^2+1.4454\times10^{-7}(T-273.15)^3 \qquad (29)$$

Mesh Generation and Boundary Conditions

Due to a rectangular structure of the fuel cell, a structured hexahedral conformal mesh is used. The resulting mesh gives high mesh orthogonal quality with almost zero skewed meshes which significantly speeds up the convergence rate.

In contrast to other work, a non-uniformly distributed grid is employed in order to accurately resolve the area of high gradient and to avoid an excessive jump in cell size within the thin layers (GDLs, CLs, and PEM) which could cause the calculation to diverge. As a result, 449664, 387328, and 533760 elements are employed for fuel cells A, B, and C, respectively. The mesh for fuel cell B is shown in **Figure 2**.

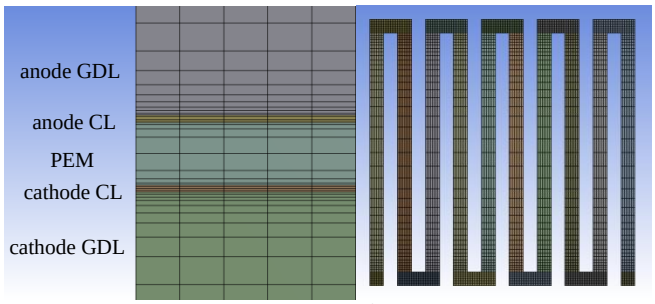

Figure 2 Side and top views of mesh used (Cell B only)

Figure 3 shows the locations where different types of boundary conditions are applied as follows:

i. Inlets: velocity inlet (u_a, u_c), mass fraction of species (H_2, H_2O at anode and O_2, H_2O at cathode), and gas temperature (T_{in})
ii. Outlets: pressure outlet
iii. Cell side walls and flow channel walls: No slip condition and zero heat flux (adiabatic wall)
iv. GDL surfaces: Potentiostatic boundary condition is applied; a constant value for steady-state simulation and varying during transient simulation.

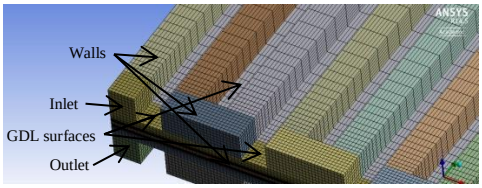

Figure 3 Boundary conditions assignment

The model properties and operating parameters used are gathered from the literature as given in **Table 2** and **Table 3**.

Table 2 Modelling parameters

Anode exchange current density [45]	80	Am^{-2}
Cathode exchange current density [45]	2×10^{-4}	Am^{-2}
H_2 reference molar concentration [45]	40.88	$molm^{-3}$
O_2 reference molar concentration [45]	40.88	$molm^{-3}$
Anode concentration exponent [44]	0.5	-
Cathode concentration exponent [44]	1	-
Anode charge transfer coefficient [44]	1	-
Cathode charge transfer coefficient [44]	1	-
H_2 reference diffusivity [44]	8×10^{-5}	m^2s^{-1}
O_2 reference diffusivity [44]	2×10^{-5}	m^2s^{-1}
H_2O reference diffusivity [44]	5×10^{-5}	m^2s^{-1}
Anode/cathode GDLs porosity [typical values]	0.5	-
Anode/cathode GDLs viscous resistance [45]	8.93×10^{13}	m^{-2}
Anode/cathode GDLs contact angle [44]	110	degree
Anode/cathode CLs porosity [44]	0.82	-
Anode/cathode CLs viscous resistance [45]	8.93×10^{13}	m^{-2}
Anode/cathode CLs contact angle [44]	110	degree
Anode/cathode specific surface active area [44]	1.25×10^{7}	m^{-1}
Membrane equivalent weight [46]	1100	$kgkmol^{-1}$
Membrane protonic conduction coefficient [46]	1	-
Membrane protonic conduction exponent [46]	1	-
Saturation exponent for pore blockage [44]	2	-

The open-circuit voltage, OCV is determined from [47];

$$V_{OCV}=1.482-0.000845T+0.0000431T\ln\left(p_{H_2}p_{O_2}^{0.5}\right) \qquad (30)$$

The mass flow rate for inlet gases at anode and cathode are given, respectively, as;

$$u_{an} = \zeta_{an} \frac{I_{ref}}{2F} \frac{A_{MEA}}{A_{ch}} \frac{RT_{an}}{y_{H_2} p_{an}} \quad (31)$$

$$u_{ca} = \zeta_{ca} \frac{I_{ref}}{4F} \frac{A_{MEA}}{A_{ch}} \frac{RT_{ca}}{y_{O_2} p_{ca}} \quad (32)$$

Table 3 Operating conditions

Parameter	A	B	C
Anode inlet velocity at 353.15 K [kgs^{-1}]	1.29	1.06	1.29
Cathode inlet velocity at 353.15 K [kgs^{-1}]	3.07	2.52	3.07
Relative humidity [RH_{an}%/RH_{ca}%]	100%/100%		
Mole fraction of H_2/H_20 at anode	0.77/0.23		
Mole fraction of O_2/H_2O at cathode	0.16/0.23		
Anode/cathode stoichiometry	3		
Operating pressure [Pa]	202650		
Anode terminal potential [V]	0		
Open-circuit voltage [V]	1.16		

RESULTS AND DISCUSSION

Validation of Numerical Model

A polarisation curve is obtained as shown in **Figure 4** to ensure the validity of the model. Despite a discrepancy in the absolute value, it is found that the predicted result agrees qualitatively and quantitatively well with the results from the experiment of Mench et al. [48]. A slight deviation from the experimental result could be explained by the fact that contact resistance between electronically conductive materials and the compression effect of the ribs on the GDLs which reduces the effective porosity of the porous layers are not accounted for. The former manifests itself as less Ohmic overpotential and therefore higher current density in the Ohmic region whereas the latter pushes the limiting current density further in the mass transport region as compared to the experimental data.

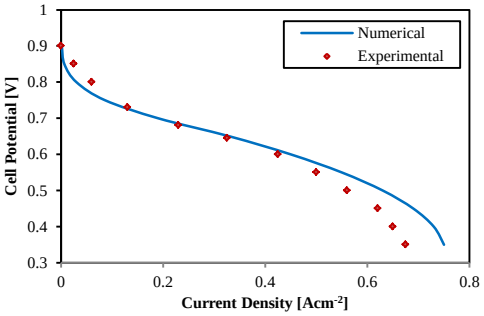

Figure 4 Operating conditions

Current Response to Step Change in Voltage

A step change in voltage from 0.70 V down to 0.50 V is applied to the three fuel cells in order to represent an extreme condition when an automotive fuel cell engine is subjected to a sudden change in power demand due to an engine start-up or high acceleration rate. It should be emphasised that all electrochemical and material parameters, and operating conditions are kept unchanged while the only difference being flow-field design parameters to obtain a fair comparison between them.

From **Figure 5**, the voltage stays at 0.70 V and then is stepped down to 0.50 V at 0.11 second. As the fuel cell potential is reduced, the electrochemical reaction becomes more active and more current are generated as seen from the plot that the three current densities increase abruptly with the presence of current overshoot at the time t = 0.12s. The three currents then decrease gradually and approach their new steady-state values of 0.94, 0.98, and 0.99 Acm^{-2} for fuel Cells A, B, and C, respectively (these are already obtained from steady-state simulation at the same operating condition). For clarity, an enlarged view at the time when the overshoot occurs is inserted in the main plot.

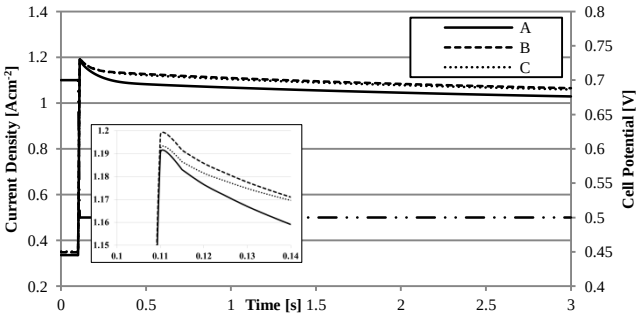

Figure 5 Current density responses due to step change in cell potential

Current Overshoot Mechanism

As suggested in the work of Shimpalee et al. [27-28] that the current overshoot is closely related to the oxygen concentration at the active catalyst layer, the time history plots of local current density and oxygen mass fraction along the lines A-A, B-B, and C-C (refer to **Figure 1**) at the cathode CL/PEM interface are given in **Figures 6-8**.

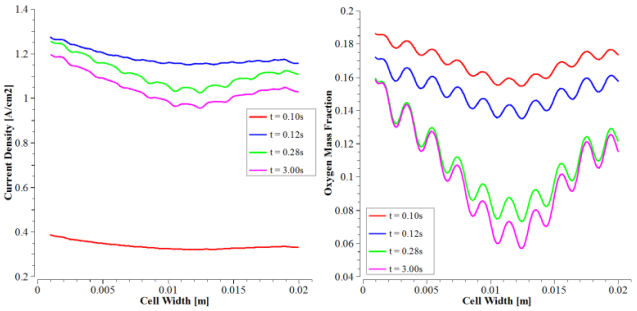

Figure 6 Local current density and oxygen distribution along line A-A

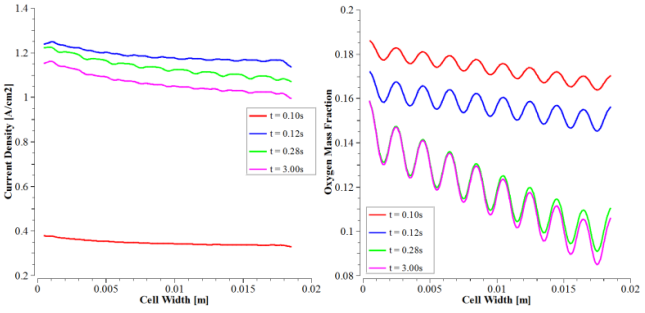

Figure 7 Local current density and oxygen distribution along line B-B

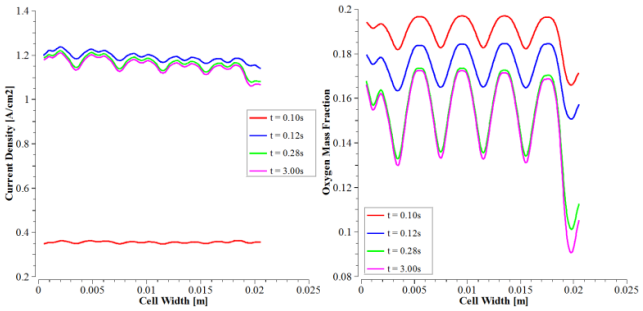

Figure 8 Local current density and oxygen distribution along line C-C

Four time instants, namely t = 0.10, 0.12, 0.28, and 3.00s are chosen to represent the instant when the voltage is initially stable prior to the voltage step down, the moment when the current overshoot occurs, the time when the current decreases rapidly after the overshoot, and when the current gradually approaches the new steady-state, respectively. It should be noted that the simulation is intentionally run for 3 seconds to save computational time and data storage and the resulting current densities of all fuel cells at 3 seconds are reported to fall well within the 10% margin of each final value. The deviations are reported to be 9.48%, 8.59%, and 6.62% for fuel Cells A, B, and C, respectively. For brevity, it is therefore justified to assume that each fuel cell has approached the new steady-state after 3 seconds.

At t = 0.10s, the voltage stays at 0.70 V and the fuel cell is in its equilibrium. The low current density is a result of low reaction with little oxygen being consumed at the active site – this is confirmed by the highest oxygen mass fraction in the right plot of **Figures 6-8**. The effect of the current collector rib that opposes the oxygen mass transport from the channel to the reaction site also manifests itself as the peaks and valleys on the oxygen mass fraction curve. Underneath the flow channel, oxygen can readily diffuse to the active layer whereas oxygen encounters high mass transport resistance due to a longer diffusing path from the flow channel to the area underneath the rib – the former results in the peaks of the mass fraction and the latter results in the valleys of the mass fraction curve.

At t = 0.12s, the current density curve is at its highest position indicating an occurrence of current overshoot. At this time instance, an excessive amount of oxygen which is already available at the active site due to an initially low reaction rate is consumed almost limitlessly by a higher reaction and results in the peak of current.

At t = 0.28s, an oxygen reservoir at the active site is used up, therefore the amount of current generated is now dependent on the ability of the flow-field to supply oxygen to the active site. Clearly, the supply of oxygen cannot catch up with the high reaction and high oxygen consumption rate at the fuel cell potential of 0.50 V. Therefore, the current density starts to decrease and gradually approach the new steady-state at t = 3.00s.

At this final stage, the local current density curve changes slightly from t = 0.28s to t = 3.00s indicating the fuel cell is approaching its new steady-state. It can be seen that oxygen is almost depleted in some parts of the active layers especially the area close to the outlet region where the mass fraction falls below 0.10.

Heat of Reaction Contour as Indicator of Local Oxygen Consumption

The local mass fraction of oxygen is the most commonly used variable in describing the local current density. According to **Equations 19-20** which suggest the current generated depends on the concentration of the oxygen at the reaction site and hence the area of high mass fraction of oxygen is believed to have high local current density accordingly. However, when the time history of the local mass fraction of oxygen as shown in **Figures 6-8** is considered, the above explanation becomes paradoxical. It is clear that at 0.1s when the current density is low, the oxygen mass fraction is redundant due to low consumption rate whereas the mass fraction is lower at 3.0s because more oxygen is consumed to maintain higher reaction kinetics. Interestingly, this contradicts the aforementioned explanation that we expect to see higher oxygen mass fraction at 3.0s, not lower. A further example of this paradox is further illustrated in **Figure 9** where current density and oxygen mass fraction contours of each cell at 0.28s are compared.

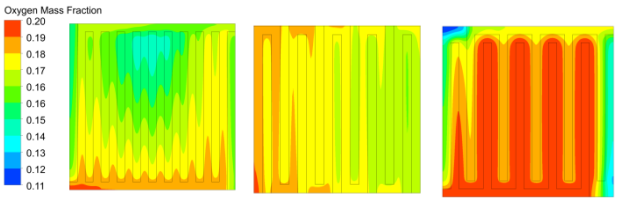

Figure 9 Oxygen mass fraction of Cells A, B, and C, respectively at 0.10 s

The averaged current densities of fuel Cells A, B, and C are 0.336, 0.348, and 0.351 Acm^{-2}, respectively. According to the explanation in **Figures 6-8**, the oxygen mass fraction of fuel Cell C should be lower than fuel Cells B and A due to the fact that more current is generated which implies more oxygen has been consumed. However, the oxygen mass fraction of fuel Cell C is highest among the three fuel cells while fuel Cell A which produces smallest current shows the lowest oxygen mass fraction.

Due to the nature of the species mass fraction, it is a relative quantity therefore its value depends on the amount of other species that coexist in each infinitesimal volume used to calculate the mass fraction. In a situation where more water vapour is being produced or transported across the membrane to the cathode side, the oxygen mass fraction can decrease due to an increase fraction of water vapour and this can sometimes be misleading giving a sense that oxygen is consumed due to a decreasing oxygen mass fraction.

Figure 10 demonstrates this effect when hydrogen is known to be consumed along the channel and hence it is expected to be depleted near the outlet area. Interestingly, the hydrogen mass fraction increases along the channel. In a PEM fuel cell operation, the proton moves across the membrane and drags the water molecules with it (electro-osmosis). The water vapour then disappears from the anode gas stream. Even though the hydrogen is also consumed and the mass fraction of it should decrease. However, the molar mass of water is much greater

than hydrogen (18 $gmol^{-1}$ versus 2 $gmol^{-1}$) more than compensates this decrease the hydrogen mass fraction therefore increases.

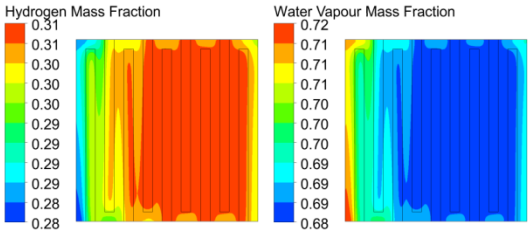

Figure 10 Hydrogen mass fraction and water vapour mass fraction at of Cell B at 1.00s (1.11 Acm^{-2}, 0.50 V)

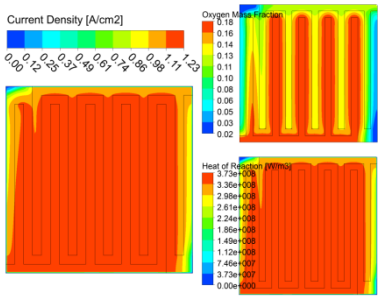

Figure 11 Comparison of oxygen mass fraction to heat of reaction as indicator Cell B at 1.00s (1.11 Acm^{-2}, 0.50 V)

The heat of reaction, on the other hand, is a direct indicator of how fast electricity is being generated by the electrochemical reaction. A higher heat means greater oxygen consumption rate. Therefore, rather than using a seemingly straightforward oxygen mass fraction contour to determine the local consumption of oxygen, the heat of reaction is a more effective indicator and should be used. This is presented in **Figure 11** for fuel Cell C at 0.30s (1.133 Acm^{-2}, 0.50 V).

To confirm that a current overshoot is a result of surplus oxygen at the reaction site, a time history of heat of reaction source for each fuel cell is given through **Figures 12-14**.

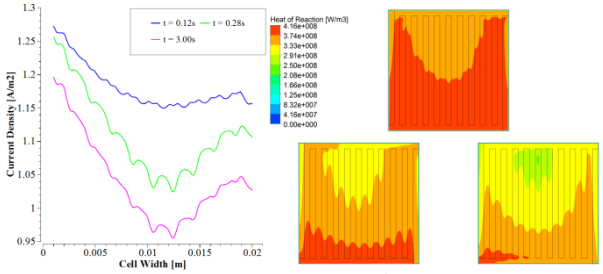

Figure 12 Cell A; 0.12s (top), 0.28s (bottom-left), and 3.00s (bottom-right)

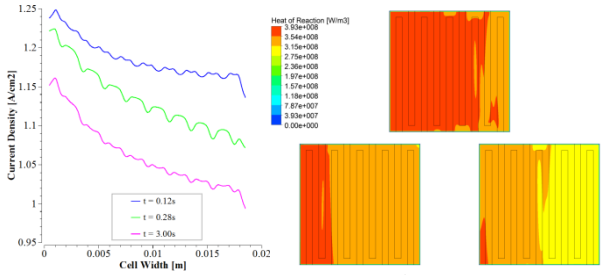

Figure 13 Cell B; 0.12s (top), 0.28s (bottom-left), and 3.00s (bottom-right)

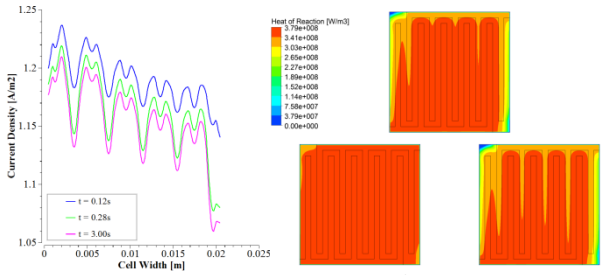

Figure 14 Cell C; 0.12s (top), 0.28s (bottom-left), and 3.00s (bottom-right)

Transient Performance Comparison of the Three Designs

Due to the nature of each flow-field design, the current density at both fuel cell potentials (0.70 V and 0.50 V) vary from one design to another. In order to examine the effect of flow-field design to the transient performance, the current densities are then normalised by the new steady-state current for a fair comparison as shown in **Figure 15**. It is found that, as a percentage of the new steady-state current density, the parallel design gives the largest current overshoot of 26% while the serpentine and interdigitated fuel cells have a overshoot of 22% and 20%, respectively.

Figure 15 also shows the averaged membrane water content at the anode and cathode sides of the membrane together with its averaged membrane protonic conductivity. Clearly, the membrane water content and protonic conductivity undergo a transition as they respond to the voltage step change and adjust to the new state but with significantly slower rate than the current response due to a much slower water diffusion and membrane water sorption/desorption mechanisms.

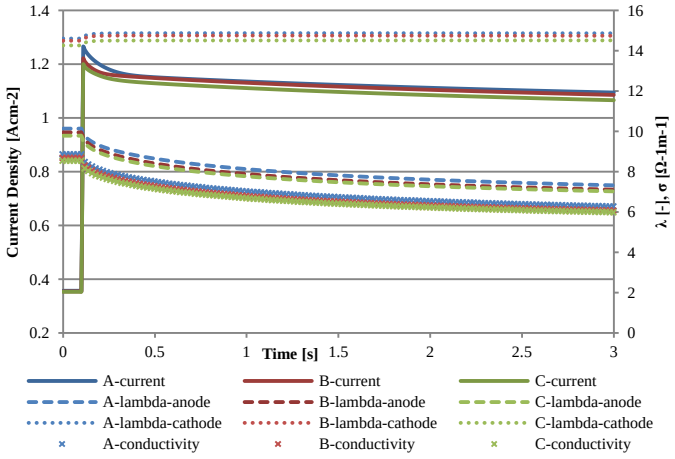

Figure 15 Normalised current density, membrane water content, and protonic conductivity of the 3 cells

The high percentage current overshoot of the parallel fuel cell can be attributed to the initially high proton conductivity of the membrane. Due to the nature of the parallel flow-field design which is known to provide inferior water removal than the serpentine or interdigitated flow-field designs, more water accumulates in the fuel cell and the membrane can absorb more water which results in higher membrane water content and protonic conductivity. **Figure 16** compares the saturation of water, *s* at the membrane/cathode catalyst layer interface at the time t = 0.10 s before the fuel cell potential is stepped down.

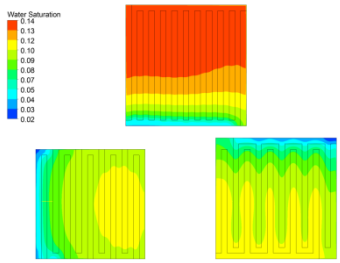

Figure 16 Water saturation; A (top), B (bottom-left), and C (bottom-right)

This might, however, seem to be advantageous in terms of membrane water content and protonic conductivity, the large current overshoot also produces heat which, in an extreme case, could cause local hotspots and deteriorate the membrane. Additionally, a large current overshoot means the time for the current to adjust to its new steady-state is lengthened and hence the fuel cell is said to have slow transient response which is undesirable from an automotive viewpoint. It is hence essential to avoid current overshoot in PEM fuel cell operation and the parallel design performs unsatisfactorily from this perspective.

In an automobile, a significant portion of power produced by the engine is consumed by a centrifugal pump that feeds the reactants to the engine and keep it running. This is also true for the case of a fuel cell engine in which two pumps are needed in order to circulate hydrogen and oxygen or air over the flow-field. A pressure drop across the flow-field is therefore not to be overlooked as it determines how much power the pump will need because higher pressure drop means higher pumping power in order to circulate the gas streams.

Figure 17 compares the pressure drop across the flow-field at the middle plane of the cathode flow field for each design. Clearly, there is significant difference in the value of pressure drop among the three designs with the interdigitated giving highest pressure drop due to its dead-ended flow channels.

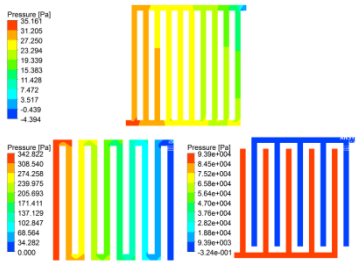

Figure 17 Pressure distribution in cathode-side flow-field; A (top), B (bottom-left), and C (bottom-right)

CONCLUSION

A 3-dimensional, 2-phase PEM fuel cell study has been carried out to investigate the transient performance of the three most commonly used flow-field designs. It is found that the fuel cell responds immediately to the change in cell potential. The current overshoot is predicted by the model as a result of the voltage step down and then it gradually adjust to the new steady-state value. The current overshoot is a result of the already available oxygen species at the reaction site which acts as oxygen reservoir so the reaction can take place almost limitlessly before the oxygen consumption exceeds the rate at which the oxygen is supplied to the reaction site which is when the current density starts to decrease and adjust to its final current density value. The parallel flow-field design produces the highest percentage current density overshoot due to the high protonic conductivity. This is however need to be avoid as large current overshoot can damage the membrane.

One important criterion for an automotive fuel cell engine is the pressure drop across the flow-field. It is shown that even though the interdigitated flow-field design outperforms the other two designs in terms of less current overshoot and time response, the dead-ended flow channels induce prohibitively high pressure drop. In a real automotive PEM fuel cell engine where a single stack contains more than 100 fuel cells and a single fuel cell is also much larger than the one in this study, for example 30 × 30 cm^2 active area, the pressure drop will be considerably higher and cannot be neglected. Therefore, the serpentine design is the best flow-field configuration as it gives a good balance between transient performance and acceptable pressure drop.

REFERENCES

[1] Djilali N., Computational modelling of polymer electrolyte membrane (PEM) fuel cell: Challenges and opportunities, *Energy*, Vol. 32, 2007, pp. 269-280

[2] Wang C.Y., Fundamental Models for fuel cell engineering, *Chemical Reviews*, Vol. 104, 2004, pp. 4727-4766

[3] Haraldsson K. and Wipke K., *Journal of Power Sources*, Vol. 126, 2004, pp. 88-97

[4] Siegel C., Review of computational heat and mass transfer modeling in polymer-electrolyte-membrane (PEM) fuel cells, *Energy*, Vol. 33, 2008, 1331-1352.

[5] Cheddie D. and Munroe N., Review and comparison of approaches to proton exchange membrane fuel cell modeling, *Journal of Power Sources*, Vol. 147, 2005, pp. 72-84

[6] Springer T.E., Zawodzinski T.A., and Gottesfeld S., Polymer electrolyte fuel cell model, *Journal of The Electrochemical Society*, Vol. 138, No. 8, August 1991, pp. 2334-2342

[7] Bernadi D.M. and Verbrugge M., A mathematical model of solid-polymer-electrolyte fuel cell, *Journal of The Electrochemical Society*, Vol. 139, No. 9, September 1992, pp. 2477-2491

[8] Bernadi D.M. and Verbrugge M., Mathematical model of a gas diffusion electrode bonded to a polymer electrolyte, *AlChE Journal*, Vol. 37, No. 8, August 1911, pp. 1151-1163

[9] Fuller T.F. and Newman J., Water and thermal management in solid-polymer-electrolye fuel cells, *Journal of The Electrochemical Society*, Vol. 140, 1993, pp. 1218-1225

[10] Nguyen T.V. and White R.E., A water and heat management model for proton-exchange-membrane fuel cells, *Journal of The Electrochemical Society, Vol.* 140, 1993, pp. 2178-2186

[11] Siegel N.P., Ellis M.W., Nelson D.J., and Von Spakovsky M.R., A two-dimensional computational model of a PEMFC with liquid water transport, *Journal of Power Sources*, Vol. 128, 2004, pp. 173-184

[12] Kazim A., Liu H.T., and Forges P., Modelling of performance of PEM fuel cells with conventional and interdigitated flow fields, *Journal of Applied Electrochemistry*, Vol. 29, 1999, pp. 1409-1416

[13] Karvonen S., Hottinen T., Saarinen J., and Himanen O., Modeling of flow field in polymer electrolyte membrane fuel cell, *Journal of Power Sources*, Vol. 161, 2006, pp. 876-884

[14] Gurau V., Liu H., and Kakac S., Two-dimensional model for proton exchange membrane fuel cells, *AlChE Journal*, Vol. 44, 1998, pp. 2410-2422
[15] Wang CY, Gu W.B., and Liaw B.Y., Micro-macroscopic coupled modelling of batteries and fuel cells, *Journal of The Electrochemical Society*, Vol. 145, 1998, pp. 3407-3417
[16] Zhou T. and Liu H., A general three-dimensional model for proton exchange membrane fuel cells, *International Journal of Transport Phenomena*, Vol. 3, No. 3, 2001, pp. 177-198
[17] Dutta S., Shimpalee S., and Van Zee J.W., Three-dimensional numerical simulation of straight channel PEM fuel cells, *Journal of Applied Electrochemistry*, Vol. 30, 2000, pp. 135-146
[18] Kim S., Shimpalee S., and Van Zee J.W., The effect of stoichiometry on dynamic behavior of a proton exchange membrane fuel cell (PEMFC) during load change, *Journal of Power Sources*, Vol. 135, 2004, pp. 110-121
[19] Kim S., Shimpalee S., and Van Zee J.W., Effect of flow field design and voltage change rate on the dynamic behavior of PEMFCs, *Journal of The Electrochemical Society*, Vol. 152, 2005, pp. A1265-A1217
[20] Kim S., Shimpalee S., and Van Zee J.W., The effect of reservoirs and fuel dilution on the dynamic behavior of a PEMFC, *Journal of Power Sources*, Vol. 137, 2004, pp. 43-52
[21] Sun H., Zhang G., Guo L., and Liu H., A study of dynamic characteristics of PEM fuel cells by measuring local currents, *International Journal of Hydrogen Energy*, Vol. 34, 2009, pp. 5529-5536
[22] Peng J., Shin J.Y., and Song T.W., Transient response of high temperature PEM fuel cell, *Journal of Power Sources*, Vol. 179, 2008, pp. 220-231
[23] Um S., Wang C.Y., and Chen K.S., Computational fluid dynamics modeling of proton exchange membrane fuel cells, *Journal of The Electrochemical Society*, Vol. 147, 2000, pp. 4485-4493
[24] Srinivasa Raju P., Prasada Raju P.V.V.N.R., Sharma K.V., and Raju B.J.J., Dynamic modeling of a PEM fuel cell, *European Journal of Scientific Research*, Vol. 43, 2010, pp. 138-147
[25] Wang Y. and Wang C.Y., Transient analysis of polymer electrolyte fuel cells, *Electrochimica Acta*, Vol. 50, 2005, pp. 1307-1315
[26] Wu H., Li X., and Berg P., Numerical analysis of dynamic processes in fully humidified PEM fuel cells, *International Journal of Hydrogen Energy*, Vol. 32, 2007, pp. 2022-2031
[27] Shimpalee S., Lee W.K., Van Zee J.W., and Naseri-Neshat H., Predicting the transient response of a serpentine flow-field PEMFC I. Excess to normal fuel and air, *Journal of Power Sources*, Vol. 156, 2006, pp. 355-368
[28] Shimpalee S., Lee W.K., Van Zee J.W., and Naseri-Neshat H., Predicting the transient response of a serpentine flow-field PEMFC II. Normal to minimal fuel and air, *Journal of Power Sources*, Vol. 156, 2006, pp. 369-374
[29] Wang Y. and Wang C.Y., Dynamics of polymer electrolyte fuel cells undergoing load changes, *Electrochimica Acta*, Vol. 51, 2006, pp. 3924-3933
[30] Shimpalee S., Spuckler D., and Van Zee J.W., Prediction of transient response for a 25-cm^2 PEM fuel cell, *Journal of Power Sources*, Vol. 167, 2007, pp. 130-138
[31] Guilin H. and Jianren F., Transient computation fluid dynamics modeling of a single proton exchange membrane fuel cell with serpentine channel, *Journal of power Sources*, Vol. 165, 2007, pp. 171-184
[32] Pasricha S. and Shaw S.R., A dynamic PEM fuel cell model, *IEEE Transactions on Energy Conversion*, Vol. 21, 2006, pp. 484-490
[33] Wang, X.D., Xu J.L., Yan W.M., Lee D.J., and Su A., Transient response of PEM fuel cells with parallel and interdigitated flow field designs, *International Journal of Heat and Mass Transfer*, Vol. 54, 2011, pp. 2375-2386
[34] Pathapati P.R., Xue X., and Tang J., A new dynamic model for predicting transient phenomena in a PEM fuel cell system, *Renewable Energy*, Vol. 30, 2005, pp. 1-22
[35] Natarajan D. and Nguyen T.V., A two-dimensional, two-phase, multicomponent, transient model for the cathode of a proton exchange membrane fuel cell using conventional gas distributors, *Journal of The Electrochemical Society*, Vol. 148, 2001, pp. A1324-A1335
[36] Loo K.H., Wong K.H., Tan S.C., Lai Y.M., and Tse C.K., Characterization of the dynamic response of proton exchange membrane fuel cells – A numerical study, *International Journal of Hydrogen Energy*, Vol. 35, 2010, pp. 11861-11877
[37] Amphlett J.C., Mann R.F., Peppley B.A., Roberge P.R., and Rodrigues A., A model predicting transient responses of proton exchange membrane fuel cells, *Journal of Power Sources*, Vol. 61, 1996, pp. 183-188
[38] Zou J., Peng X.F., and Yan W.M., Dynamic analysis of gas transport in cathode side of PEM fuel cell with interdigitated flow field, *Journal of Power Sources*, Vol. 159, 2006, pp. 514-523
[39] Najjari M., Khemili F., and Nasrallah S.B., The effect of the gravity on transient responses and cathode flooding in a proton exchange membrane fuel cell, *International Journal of Hydrogen Energy*, Vol. 38, 2013, pp. 3330-3337
[40] Andreassi L., Cordiner S., and Romanelli F., Performances analysis of PEM fuel cell based automotive systems under transient conditions, *SAE Techincal Paper 2003-01-1144*, 2003, pp. 245-258
[41] Le A.D. and Zhou B., A general model of proton exchange membrane fuel cell, *Journal of Power Sources*, Vol. 182, 2008, pp. 197-222
[42] Choopanya P. and Peng Z., An investigation on steady-state performance of conventional and serpentine flow-fields for automotive polymer electrolyte membrane fuel cell, *SCODECE Internal Conference/International Forum on Vehicle Control*, 2012
[43] Peng Z. and Choopanya P., CFD investigation into internal flows of PEM fuel cell for optimal performances, *Advanced Materials Research*, Vol. 724-725, 2013, pp. 757-761
[44] Iranzo A., Munoz M., Rosa F., and Pino J., Numerical model for the performance prediction of a PEM fuel cell cell. Model results and experimental validation, *International Journal of Hydrogen Energy*, Vol. 35, 2010, pp. 11533-11550
[45] Ju H. and Wang C.Y., Experimental validation of a PEM fuel cell model by current distribution data, *Journal of The Electrochemical Society*, Vol. 151, 2004, pp. A1954-A1960
[46] PEMFC and Electrolyte Add-on Module User Guide, Release 12.0, ANSYS Inc., January 23, 2009
[47] PEM Fuel Cells: Theory and Practice, Frano Barbir, Academic Press, July 2005
[48] Mench M.M., Wang C.Y., and Ishikawa M., In situ current distribution measurements in polymer electrolyte fuel cells, *Journal of The Electrochemical Society*, Vol. 150, 2003, pp. A1052-A1059